UDK/*UDC*: 519.6:627.82(078.7)
Izvirni znanstveni članek – *Original scientific paper*
DOI: 10.15292/acta.hydro.2025.06

Prejeto/*Received:* 07.07.2025
Sprejeto/*Accepted:* 14.01.2026
Objavljeno na spletu/*Published online:* 03.02.2026

NUMERICAL SIMULATION OF DAM-BREAK FLOW USING A MODIFIED RUNGE-KUTTA SCHEME WITH VALIDATION

NUMERIČNA SIMULACIJA TOKA OB PORUŠITVI PREGRADE Z UPORABO MODIFICIRANE SHEME RUNGE-KUTTA Z VALIDACIJO

Lamia Touazi[1], Tahar Ikni[1], Ali Berreksi[1]

[1]Université de Bejaia, Faculté de Technologie, Département d'Hydraulique, Laboratoire de Recherche en Hydraulique Appliquée et Environnement (LRHAE), 06000, Bejaia. Algérie

Abstract

This paper presents a numerical scheme based on the second-order Runge–Kutta method, combined with finite-difference spatial discretisation, for simulating dam-break flows governed by the one-dimensional Saint-Venant equations. The proposed method introduces a flow decomposition coupled with an artificial viscosity term inspired by previous work, in order to improve the numerical stability and accuracy of the results. A comparative analysis is carried out between the classical scheme and the modified Runge–Kutta second-order scheme using an analytical solution as a reference. The results show that the modified scheme is significantly better matched to the analytical solution. The method is then applied to several dam failure scenarios including complex conditions such as triangular and trapezoidal obstacles, sloping bottoms and dry bed/wet bed transitions. The numerical results are compared with experimental data and simulation results published in the specialist literature. In all cases, the modified scheme performs better confirming its robustness and accuracy for modelling the propagation of dam burst waves under complex hydraulic conditions.

Keywords: Dam-break, Saint-Venant, Modelling, Runge–Kutta classical scheme, Friction, Runge–Kutta modified scheme.

Izvleček

V članku je predstavljena numerična shema, ki temelji na metodi Runge–Kutta drugega reda v kombinaciji s prostorsko diskretizacijo z metodo končnih razlik za simulacijo tokov ob porušitvi pregrade, ki jih opisujejo enodimenzionalne Saint-Venantove enačbe. Predlagana metoda uvaja razdelitev toka v kombinaciji z umetnim, viskoznim členom, ki temelji na prejšnjem delu, da bi se izboljšala numerična stabilnost in natančnost rezultatov. Izvedena je primerjalna analiza med klasično in modificirano shemo Runge–Kutta drugega reda, pri čemer se kot referenca uporabi analitična rešitev. Rezultati kažejo, da se modificirana shema bistveno bolje ujema z analitično rešitvijo. Metoda se nato uporabi za več scenarijev porušitve pregrade, vključno z zahtevnimi pogoji, kot so trikotne in trapezne ovire, nagnjeno dno in prehodi med suhim in mokrim

[1] Stik / *Correspondence*: lamia.touazi@univ-bejaia.dz

dnom. Numerični rezultati so primerjani z eksperimentalnimi podatki in rezultati simulacij, objavljenimi v strokovni literaturi. V vseh primerih se modificirana shema izkaže kot učinkovitejša, kar potrjuje njeno robustnost in natančnost pri modeliranju širjenja vala ob porušitvi pregrade v zahtevnih hidravličnih pogojih.

Ključne besede: porušitev pregrade, Saint-Venant, modeliranje, klasična shema Runge–Kutta, trenje, modificirana shema Runge–Kutta.

1. Introduction

A dam is an artificial or natural structure built across the bed of a watercourse that retains or is capable of retaining water. Dams have various functions, including regulating watercourses (flood control in periods of high water, maintaining a minimum water level in periods of drought), irrigating crops, supplying water to towns, generating electricity, developing tourism and fighting fires (Ikni et al., 2024a and 2024b). The failure of a water retention structure generally generates a rapid increase in water flows, resulting in significant and dangerous flooding and causing damage to rivers in the hydrographic network downstream of the dam (Cannata and Marzocchi, 2012; Azeez et al., 2020, Lim et al., 2024). The history of previous failures obliges dam safety specialists to take into account the possibility of huge water releases, which can exceed common natural floods (Hsu and Yeh, 2002; Soleymani et al., 2015). The submersion wave, by its intrinsic force, causes considerable destruction downstream of the dam. It is tracked by a significant flood, combining the water and debris from the dam, and severe erosion of the river valley. Such an event has very dangerous consequences for people living downstream of the dam (Zokagoa and Soulaïmani, 2010; Pilotti et al., 2011). The consequences for property also may vary from simple damage to the total demolition of roads, homes, and other structures (Al-Ansari et al., 2015). If other dams are present downstream, the submersion wave can in turn cause them to break and thus accentuate the damage. In order to apply appropriate safeguard measures to mitigate potential flood impacts, researchers are required to develop physical models of the flows generated by floods (Berreksi et al., 2022). The development and improvement of numerical simulation models will make it possible to estimate flow parameters (height, velocity and discharge) more accurately, with the aim of elaborating flood maps (Chen et al., 2005; You et al., 2012).

Recently, considerable research has been conducted on dam-break waves in various contexts, including flows over slopes, with or without friction, and on dry or wet beds, as well as in the presence of obstacles with different shapes**.** In this context, Bellos and Hrissanthou (2011) have used Lax–Wendroff and MacCormack finite-difference schemes in order to calculate the dam-break problem with the presence of a triangular obstacle. Both schemes yielded practically identical results. This same phenomenon was studied by Wu et al. in 2014, where the finite volume method was used to resolve the two dimensional equations system of free-surface flows. Magdalena and Pebriansyah (2022) studied the dam-break wave on various obstacles: triangular, trapezoidal and rectangular. They applied four finite-difference schemes to solve the one-dimensional Saint-Venant equation. Maghsoodi et al. (2022) analysed the dam-break wave with ANSYS Fluent 6.3.26 using the 3D Reynolds equations. Computer modelling of dam-break flow over different obstacles is carried out on a dry bed. Dam-break wave calculation with the presence of a singularity was undertaken by Rahou and Korichi (2023) using the two dimensional Saint-Venant equations.

Building on these works, the present study presents a significant methodological advancement through a modified explicit second-order Runge–Kutta scheme. Our innovative approach combines an original decomposition of the flux term with the introduction of an adapted artificial viscosity, which enhances control over numerical oscillations and improves the accuracy of transient flow simulations, especially in the presence of sharp discontinuities. This method effectively complements and advances existing numerical techniques for dam-break modelling.

The main objective of this study is to conduct a rigorous comparative study. The proposed scheme is first benchmarked against the classical Runge–Kutta method, using Stoker's (1957) analytical solution to demonstrate its improvements. It is subsequently validated on several complex cases from the literature, including scenarios with or without friction, various obstacle geometries (triangular, trapezoidal), dry/wet bed transitions, and dam-breaks on inclined slopes, proving its superior robustness and accuracy.

Methodology

2.1 Basic equations

Free-surface flows can be unsteady, steady, supercritical, critical or subcritical. These flows can be described by the 1D Saint-Venant equations. These equations are obtained by applying the two principles of dynamics: the principle of continuity and momentum principle (Chanson, 2005):

$$\begin{cases} \frac{\partial h}{\partial t} + \frac{\partial (hu)}{\partial x} = 0 \\ \frac{\partial (hu)}{\partial t} + \frac{\partial}{\partial x}(hu^2 + \frac{1}{2}(gh^2)) = gh(S_0 - S_f) \end{cases} \quad (1)$$

with h the water depth, S_0 the channel bottom slope, S_f the friction slope, and u the depth-averaged velocity.

For a horizontal channel and an ideal fluid, equation (1) is written as (Chanson, 2004; Castro-Orgaz and Chanson, 2017):

$$\begin{cases} \frac{\partial h}{\partial t} + \frac{\partial (hu)}{\partial x} = 0 \\ \frac{\partial (hu)}{\partial t} + \frac{\partial}{\partial x}(hu^2 + \frac{1}{2}(gh^2)) = 0 \end{cases} \quad (2)$$

In this study, we focus directly on the conservative form of the one-dimensional Saint-Venant equations, expressed as:

$$\frac{\partial V}{\partial t} + \frac{\partial F(V)}{\partial x} = S \quad (3)$$

$$V = \begin{pmatrix} h \\ hu \end{pmatrix};\ F = \begin{pmatrix} hu \\ hu^2 + \frac{1}{2}gh^2 \end{pmatrix};\ S = \begin{pmatrix} 0 \\ gh(S_o - S_f) \end{pmatrix} \quad (4)$$

with V the vector of conservative variables, $F(V)$ the flux vector and S the source vector. The components of S (S_o and S_f) are given by:

$$S_o = \sin(\alpha_x) \quad (5)$$

$$S_f = \frac{u|u|n^2}{h^{4/3}} \quad (6)$$

where α_x is the slope angle of channel's bottom according to the x direction, and n the Manning's roughness coefficient.

In the remainder of the manuscript, we uniformly use h to denote the water depth and u to denote the depth-averaged velocity, and we explicitly adopt the conservative variables V and F. All numerical developments and simulations rely exclusively on this conservative formulation.

Note: Equations (1) and (2) are recalled to introduce the fundamental principles of continuity and momentum conservation.

2.2 Numerical resolution method

The numerical solution proceeds in two steps: spatial discretization of the partial differential equations system (PDEs) using finite difference methods, followed by time integration using the Runge–Kutta scheme.

Generally speaking, it is very difficult, if not impossible, to solve the Saint-Venant system of equations analytically. Consequently, a numerical resolution of these equations is essential. To numerically solve the one-dimensional Saint-Venant system to study the dam-break problem, two finite difference numerical schemes are used. These are the second-order Runge–Kutta and modified second-order Runge–Kutta schemes.

The second-order Runge–Kutta numerical scheme used in this study has already been combined with finite difference spatial discretization in previous works.

The newly proposed "Modified Runge–Kutta" scheme does not alter the time integration method itself; rather, it represents a global improvement of the existing numerical framework. It refers to a scheme explicitly constructed by combining:

- A second-order Runge–Kutta time integration (unchanged) with finite difference spatial discretization,
- A weighting factor θ, interpreted as an artificial viscosity in the sense of Bellos & Hrissanthou (2011), Garcia-Martinez et al., (2009), Zendrato

et al.,(2019) and Maitsa et al., (2020), acting as a numerical regularization to control spurious oscillations,

- And, above all, a new contribution introduced in this work: the decomposition of the convective flux term $\partial F/\partial x$ into two components discretized through a predictor and corrector central difference scheme**.**

This decomposition helps reduce numerical oscillations and better reproduce the actual shape of dam-break waves, without resorting to more complex methods such as finite volume approaches.

Runge–Kutta second-order scheme

The second-order Runge–Kutta scheme, in time and space, is composed of two computational steps: a Prediction step and a Correction step (Torbi et al., 2019; Tseng & Chu, 2000):

Prediction step

$$V_i^P = V_i^n - \frac{\Delta t}{4\Delta x}\left[F_{i+1}^n - F_{i-1}^n\right] + 0.5\Delta t S_i^n \quad (7)$$

Correction step

$$V_i^{n+1} = V_i^n - \frac{\Delta t}{2\Delta x}\left[F_{i+1}^P - F_{i-1}^P\right] + \Delta t S_i^p \quad (8)$$

Following the approach of Bellos & Hrissanthou (2011), we replaced in equations (7) and (8) the term V_i^n by a first-order numerical filter (artificial viscosity), defined as, $\theta V_i^n + 0.5(1-\theta)(V_{i+1}^n + V_{i-1}^n)$, and we obtained equations (9) and (10).

The parameter θ acts as a smoothing factor on the conservative variables during the prediction and correction steps, helping to control numerical diffusion and reduce oscillations. It should be emphasized that this artificial viscosity does not represent any physical dissipation but corresponds to a purely numerical regularization mechanism, inspired by the digital filters proposed by Bellos & Hrissanthou (2011).

Prediction step

$$V_i^P = \theta V_i^n + 0.5(1-\theta)(V_{i+1}^n + V_{i-1}^n) - \frac{\Delta t}{4\Delta x}[F_{i+1}^n - F_{i-1}^n] + 0.5\Delta t S_i^n \quad (9)$$

Correction step

$$V_i^{n+1} = \theta V_i^n + 0.5(1-\theta)(V_{i+1}^n + V_{i-1}^n) - \frac{\Delta t}{2\Delta x}[F_{i+1}^P - F_{i-1}^P] + \Delta t S_i^P \quad (10)$$

with θ introduced as a weighting parameter ranging between 0 and 1 ($0 \le \theta \le 1$), which ensures stability during the prediction and correction steps of the Runge–Kutta scheme. In this study, θ =0.55 was adopted for the classical Runge–Kutta scheme (equations (9) and (10)) and θ =0.73 for the modified Runge–Kutta scheme (equations (11) and (12)), based on sensitivity analyses.

The main innovation of this work lies in the treatment of the spatial flux term. The classical expression $\frac{F_{i+1}^n - F_{i-1}^n}{2\Delta x}$ is replaced by:

$$\frac{1}{\Delta x}[\theta(F_i^n - F_{i-1}^n) + (1-\theta)(F_{i+1}^n - F_i^n)] \quad (10a)$$

The convective fluxes *F* are discretized using this decomposed central difference scheme, which is specifically designed to balance accuracy and numerical stability. This approach, coupled with the artificial viscosity term, effectively damps out spurious oscillations and handles sharp discontinuities typical of dam-break flows without resorting to more complex finite volume or flux limiting methods.

The new Runge–Kutta formulation after decomposition of the flow term is:

Prediction step

$$V_i^P = \theta V_i^n + 0.5(1-\theta)(V_{i+1}^n + V_{i-1}^n) - \frac{\Delta t}{2\Delta x}[\theta(F_i^n - F_{i-1}^n) + (1-\theta)(F_{i+1}^n - F_i^n)] + 0.5\Delta t S_i^n \quad (11)$$

Correction step

$$V_i^{n+1} = \theta V_i^n + 0.5(1-\theta)(V_{i+1}^n + V_{i-1}^n) - \frac{\Delta t}{\Delta x}[\theta(F_i^P - F_{i-1}^P) + (1-\theta)(F_{i+1}^P - F_i^P] + \Delta t S_i^P \quad (12)$$

The formulation used to calculate the time step is (Garcia-Navarro et al., 2008):

$$\Delta t \le \mathrm{CFL}\frac{\Delta x}{\max(h_i + \sqrt{g h_i})} \quad \text{with CFL} < 1 \quad (13)$$

This equation is employed to ensure the stability of the numerical scheme used.

2.3 Treatment of specific numerical aspects

In addition to the treatment of convective fluxes, specific numerical aspects were implemented to ensure the scheme's stability, accuracy, and

conservation properties. These include wet and dry treatment, boundary condition treatment, and source term discretization for variable bed slopes, as detailed below.

a) Wet and dry treatment

To ensure numerical stability and mass conservation when wetting and drying occur, a minimum water depth threshold of $h_{min}=1\times10^{-5}$ m was adopted (Mohapatra & Bhallamudi, 1996). This threshold is applied only to outgoing fluxes: when $h < h_{min}$, fluxes are cancelled and the local velocity is set to zero, thus avoiding non-physical exchanges, division by zero, and mass loss.

b) Boundary conditions

Three types of boundary conditions were explicitly implemented in this work:

- **Dam-break on a horizontal bed:** free conditions**,** based on the linear extrapolation of hydraulic variables from inner cells (Das and Bagheri, 2015; Ikni et al., 2018).

$$\begin{cases} V_i^{n+1} = 2V_2^{n+1} - V_3^{n+1} \\ V_N^{n+1} = 2V_{N-1}^{n+1} - V_{N-2}^{n+1} \end{cases} \quad (14)$$

- **Dam-break with obstacle:** reflective boundary conditions (Gu et al., 2017).

$$\begin{cases} h_1^{n+1} = h_2^{n+1} \\ u_1^{n+1} = -u_2^{n+1} \\ h_N^{n+1} = h_{N-1}^{n+1} \\ u_N^{n+1} = -u_{N-1}^{n+1} \end{cases} \quad (15)$$

- **Dam-break on an inclined bed:** free boundary conditions similar to the horizontal case, but accounting for the bed slope in the extrapolation of the variables.

c) Source term treatment

The source term includes the bed slope S_0 and the friction slope S_f. In this study, a continuous bed profile $S_0 = sin(\alpha x)$ was considered, while the general form $S_0 = -\partial z_b/\partial x$ also applies to irregular topographies. Under the lake-at-rest condition ($u=0$, $\eta=h+z_b=const$), the flux gradient and source term balance, ensuring the was well-balanced and avoiding spurious velocities.

3. Case study

This section is devoted to validating the numerical model elaborated. To this end, three case studies were carried out. The first application concerns the flow caused by a dam-break at a wet horizontal bottom in which the friction is neglected. In the second application, the effect of friction is considered. The third application deals with the simulation of a dam failure in the presence of a triangular barrier into a channel with friction.

3.1 Dam-break in the case of a horizontal wet and frictionless bed

The present test involves a flow due to the dam-break wave situated in the middle of the channel (L=1m, x=0.5L), with L represents the global length of the channel. The upstream (ups) water depth of the dam is h =1m, and the downstream (dwn) water depth is h =0.1m (Fig. 1).

A structured mesh of 1000 nodes is used for numerical simulations. A complete and instantaneous collapse of the dam is assumed. This case is considered in order to test the robustness of the two numerical schemes used.

Figure 2 shows, respectively, the analytical and numerical simulation results at t=0.1 second after the dam break.

It can be seen from Figure 2 that the numerical simulation results converge with Stoker's analytical solution (Stoker, 1957) for both versions of the Runge–Kutta and modified Runge–Kutta schemes (Figures 2a and 2b). The obtained results show that the new formulation of the flux term (eqs.11 and 12) gives better simulations (Figure 2). Table 1 summarizes the values of the parameters used (spatial discretization step Δx, Courant–Friedrichs–Lewy number CFL, and weighting parameter θ) to calibrate Stoker's analytical solution with both the classical and modified Runge–Kutta schemes. The values of CFL and θ reported in the table correspond to the maximum values used.

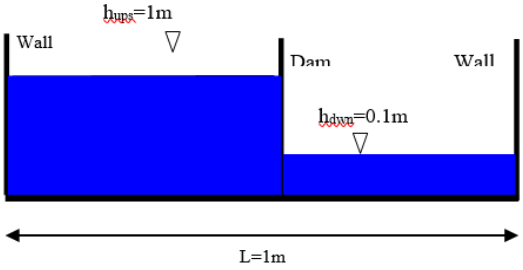

Figure 1: *Dam-break flow on a wetted bed.*

Slika 1: *Pretok ob porušitvi pregrade po mokrem dnu.*

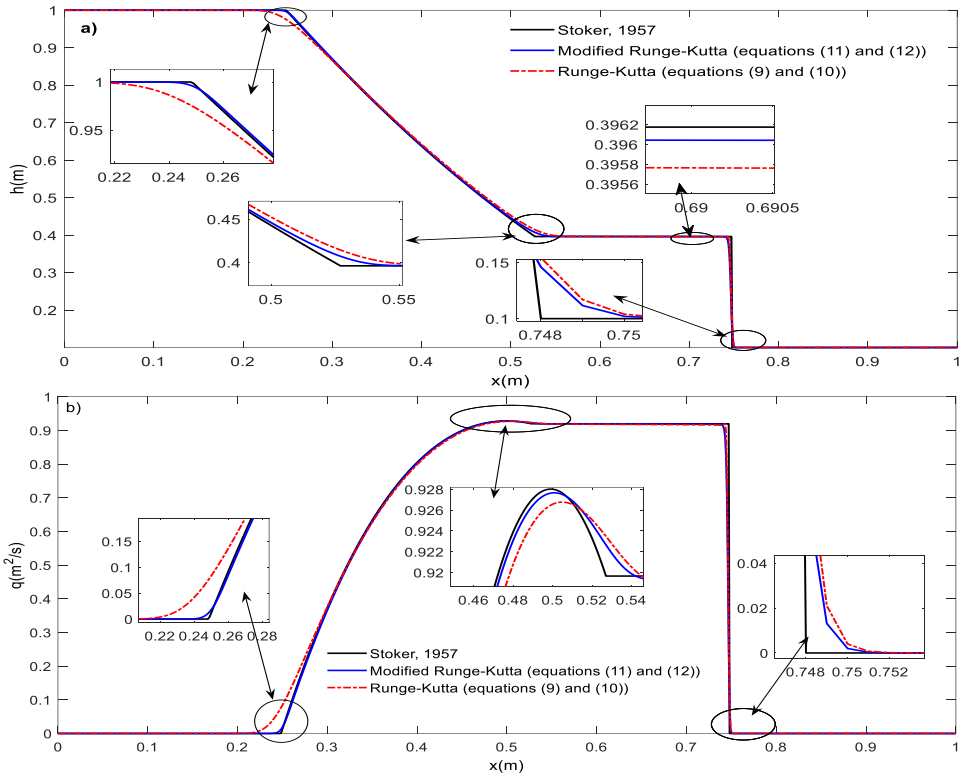

Figure 2: *Analytical and simulated results for depth ratio h_{dwn} /h_{ups}= 0.1 and t=0.1s: a) water depth h (m); b) unit flow rate q=uh (m^2/s).*

Slika 2: *Analitični in simulirani rezultati za razmerje globin h_{dwn} /h_{ups}= 0,1 in t=0,1s:* ***a)*** *globina vode h (m);* ***b)*** *enotni pretok q=uh (m^2/s).*

The calculation of first-order relative error (ER) between the analytic and simulated solution is presented below, using the following formula (Kirstetter et al., 2021):

$$ER = \frac{\sum_1^N |h_{simul,i} - h_{analyt,i}|}{N} \quad (14)$$

where N represents the grid points number. The values of ER are grouped in table 2 below. The new formulation of the Runge–Kutta scheme (equations (11) and (12)) generates a lower error compared to the classical Runge–Kutta scheme (equations (9) and (10)) for the same depth ratio. The table indicates that the modified Runge–Kutta scheme yields the best outcomes.

Table 1: *Values of the parameters used (spatial discretization step Δx, Courant–Friedrichs–Lewy number CFL, and weighting parameter θ).*

Preglednica *1: Vrednosti uporabljenih parametrov (prostorski diskretizacijski korak Δx, Courant–Friedrichs–Lewyjevo število CFL in utežni parameter θ).*

h_{dwn}/ h_{ups}=0.1	**Δx (m)**	**CFL**	**θ**
Runge–Kutta (Equations (9) and (10))	0.001	0.85	0.55
Runge–Kutta modified (Equations (11) and (12))	0.001	0.95	0.73

Table 2: *Relative error (ER).*

Preglednica 2*: Relativna napaka (ER).*

	Runge–Kutta Equations (9) and (10)	Modified Runge–Kutta Equations (11) and (12)	Error report
ER (h_{dwn}/h_{ups}=0.1)	**0.0027**	**0.000981**	**2.7523**

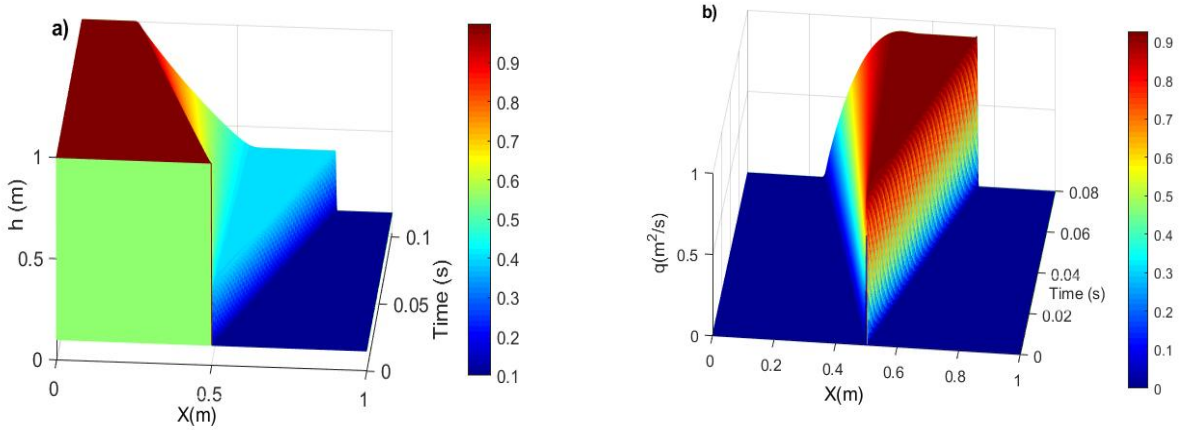

Figure 3: *Three-dimensional representation:* ***a)*** *Water depth variation h (m) according to time and* ***b)*** *Unit flow variation q=uh (m^2/s) versus time*

Slika 3: *Tridimenzionalni prikaz:* ***a)*** *spreminjanje globine vode h (m) glede na čas in* ***b)*** *spreminjanje enotnega pretoka q=uh (m^2/s) glede na čas*

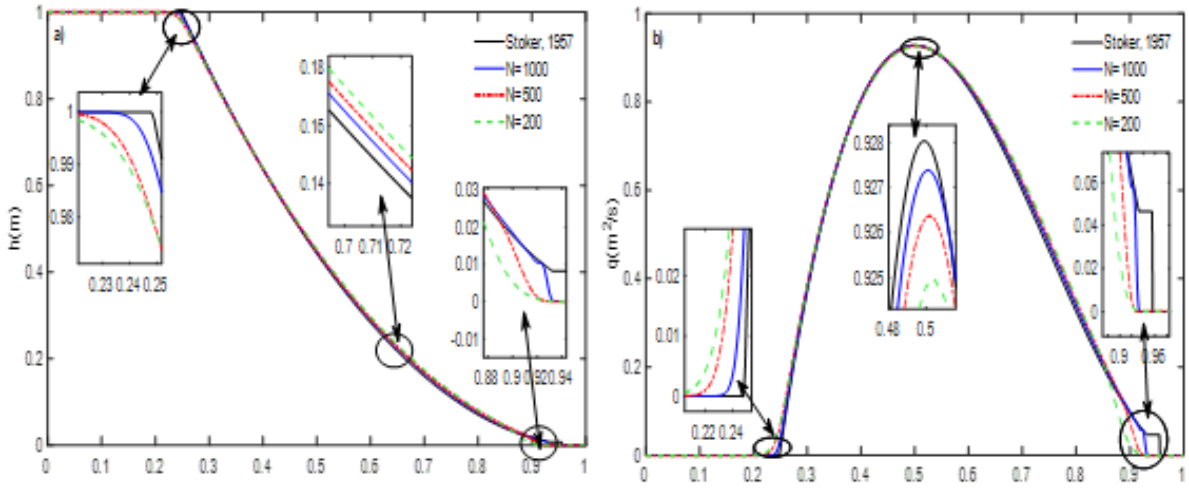

Figure 4: *Effect of the number of discretization points on the solution (N=200, N=500, and N=1000.*

Slika 4: *Vpliv števila točk diskretizacije na rešitev (N=200, N=500 in N=1000).*

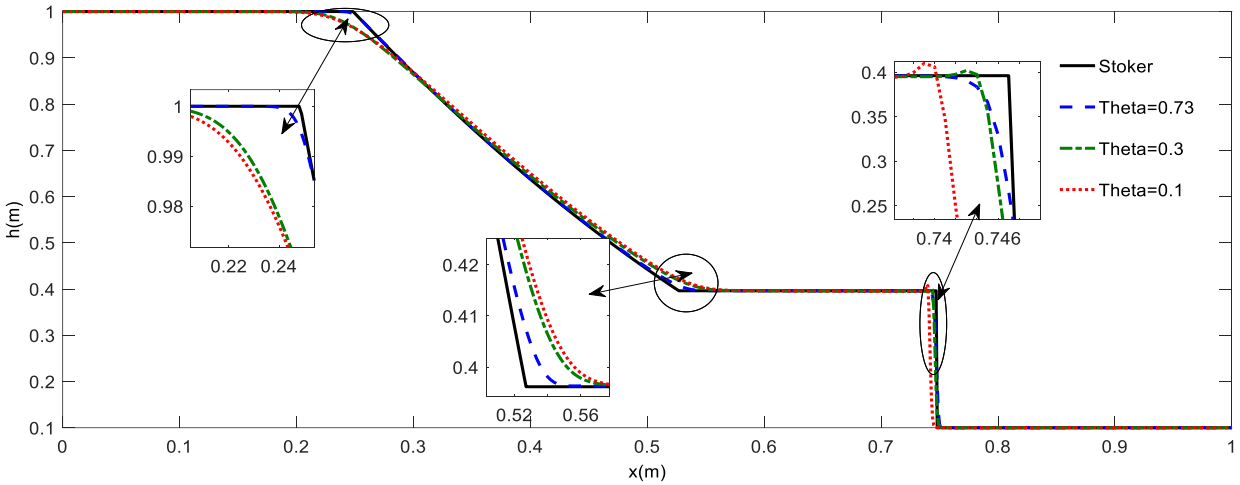

Figure 5: *Water height h at t=0.08 s: (θ =0.1, θ =0.3, and θ =0.73).*

Slika 5: *Višina vode h pri t=0,08 s: (θ =0,1, θ =0,3 in θ =0,73).*

Table 3: *Error as a function of parameter θ.*

Preglednica 3*: Napaka kot funkcija parametra θ.*

CFL	Values of θ	Time (s)	Error
0.95	0.73	0.08	0.000981
	0.3		0.004
	0.1		0.0053

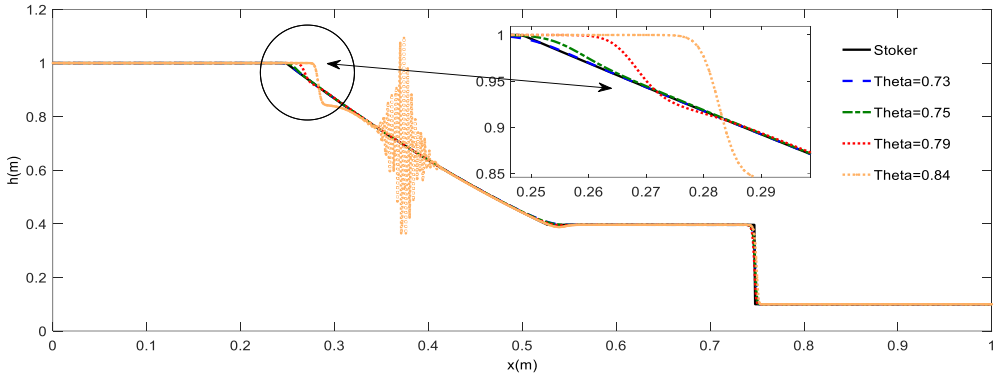

Figure 6: *Water height h at t=0.08 s: (θ =0.73, θ =0.75, θ =0.79, and θ =0.84).*

Slika 6: *Višina vode h pri t=0,08 s: (θ =0,73, θ =0,75, θ =0,79 in θ =0,84).*

From this section onwards, the modified Runge–Kutta scheme (equations (11) and (12) is used in all the applications studied.

Fig. 3 shows a three-dimensional view of water level variation h (m), and unit flow q=uh (m^2/s) as a function of time. Fig. 3a and 3b clearly show the wave front displacement and the unit flow in the channel versus time.

Effect of the number of discretisation points (N)

The effect of the discretization points number (N) on the solution's accuracy is shown in Figure 4. Figure 4a and 4b show, respectively, the variation in water level and unit flow along the canal after the dam has broken. These figures clearly show that the solution's accuracy increases with the increase in the number of discretization points (N). For N=1000, the solution is better (Figures 4a and 4b).

Effect of parameter θ on the calibration of numerical results

Figure 5 shows the simulated and analytical depth profiles at t= 0.08s. This figure clearly illustrates that the calibration depends on parameter θ. Table 3 shows that the error decreases as the value of parameter θ increases up to a limit value (in our case θ =0.73).

When the value of parameter θ exceeds the calibration limit (θ=0.73), the second-order Runge–Kutta scheme loses its stability and convergence, as shown in Figure 6. The numerical solution shifts to the right of the analytical solution.

3.2 Dam-break phenomenon in a horizontally sloped surface under friction

Dam-break flow on a dry bottom with friction was studied by Schoklitsch (1917). The experimental test bench consists of a channel 20 m long, 0.08 m high, and 0.096 m wide (Fig. 7). The gate, which acts like a dam, is positioned in the canal's middle (at x=10m). At the upstream (ups) gate, the water level is 0.074m, but there is no water level downstream (dwn). The value of Manning's rugosity factor employed in this test is 0.009 $s/m^{1/3}$. The experimental results of Schoklitsch (1917) were used by Lai and Khan (2012) to validate the results of their numerical simulation using the finite element technique. The channel length is divided into in 200 segments. The Courant-Friedrichs-Lewy (CFL) condition (equation (13) is used to calculate the time step Δt.

The experimental water surface profile obtained by Schoklitsch (1917), those calculated by Lai and Khan (2012) and that simulated while using the modified Runge–Kutta scheme (equations (11) and (12)) at t=3.75 seconds and t=9.4 seconds after dam-break are shown in Fig. 8. A good fit is observed between the water surface profile calculated with the present model and the experimental one. The first clearly shows that the wave front displacement is well simulated with the numerical model proposed compared to that reproduced by Lai and Khan (2012).

These figures also show that the wave front displacement depends on friction. For an ideal fluid,

the front position is at x=16m at T=3.75s and at x>20m at T=9.4s (Figures 8a and 8b). In contrast, for a real fluid, the front position is x<16m at T=3.75s and x<18m at T=9.4s (Figure 8a and 8b). These figures clearly illustrate that the wave front's movement speed for an ideal fluid is greater than that for a real fluid. These results clearly show that the approach employed in the actual research work is suitable for describing the wave propagation after the dam-break in an initially frictional dried bottom.

The 3D representation of the water level changes versus time is presented in Figure 9. The curves given in the figure in question clearly illustrate the wave front displacement in the channel according to time for a real fluid (Figure 9a) and for an ideal fluid (Figure 9b).

3.3 Dam break in the case of a triangle-shaped obstruction

This part compares the obtained findings using the proposed numerical model (equations (11) and (12)) with the measurements of the dam-break wave propagation in the case of a triangle-shaped obstruction and other results computed by Wu et al. (2014). Figure 10 gives the describing of the dam-break experiment in the existence of an obstruction (IMPACT project, 2001). The upstream entrance to the 5.6-meter-long canal is 2.39 meters from the dam. A 0.9 m wide by 0.065 m high triangular barrier is erected downstream of the dam site (Bellos and Hrissanthou, 2011; Wu et al., 2014).

A wet boundary is formed on the closed downstream end of the channel by the retention of 0.02 meters behind the triangular obstruction and the 0.111 meters of water height upstream of the dam (Fig. 10). Downstream of the dam, there are three points of water depth measurements located at G1 (1.545 m), G2 (2.535 m) and G3 (3.185 m) (Wu et al., 2014). The channel width and the roughness coefficient used here are respectively on the order of 0.5 m and 0.011 $s.m^{-1/3}$. Wu et al. (2014), applied the finite volume technique to compute this phenomenon via the 2D flow equations system. The measurements and computed water levels obtained by Wu et al. (2014) at G1, G2, and G3 locations are used to approve the results achieved using the modified Runge–Kutta scheme (equations 11 and 12).

The experimental water depths and those calculated by Wu et al. (2014), as well as the heights simulated via the numerical model developed in the present study (equations (11) and (12)), are shown in Figure 11. The identical Δx discretization step is used (Δx=0.01 m) with a CFL number equal to 0.95.

It is easy to deduce that the proposed new technique simulates the experimental results well. Indeed, a good adequacy between the simulated values and the experimental measurements is observed. This is clearly illustrated in Figures 11a, 11b, and 11c.

Figure 12 combines the experimentally measured water levels, those computed by Wu et al. (2014) and those performed by means of the modified Runge–Kutta scheme (equations (11) and (12).

The two simulation results show a good fit between the experimental results and those computed by the elaborated numerical model and those calculated by Wu et al. (2014). Figures 12c and 12b show that the obtained results are slightly better than those obtained by Wu et al. (2014).

At the spikes as shown in Figure 13, the modified Runge–Kutta scheme simulates the experimental results better than those obtained by Wu et al. (2014).

The 3D representation of water depth variation at t=6 s is presented in Figure 14. This final stage of the simulation summarizes the overall wave evolution, including its interaction with the obstacle and the downstream wall. It captures the key hydrodynamic phenomena that occurred throughout the simulation, such as the wave front propagation, overtopping of the obstacle, the formation of a hydraulic jump, and the reflection from the downstream boundary, followed by the return flow upstream of the obstacle.

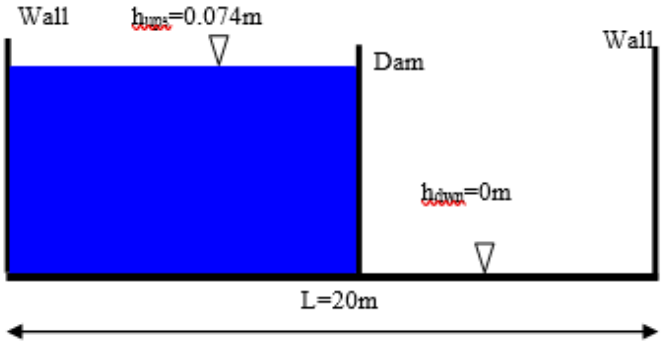

Figure 7: *Flow in the case of a dam-break on a flat dried bottom.*

Slika 7: *Pretok v primeru porušitve pregrade po nenagnjenem suhem dnu.*

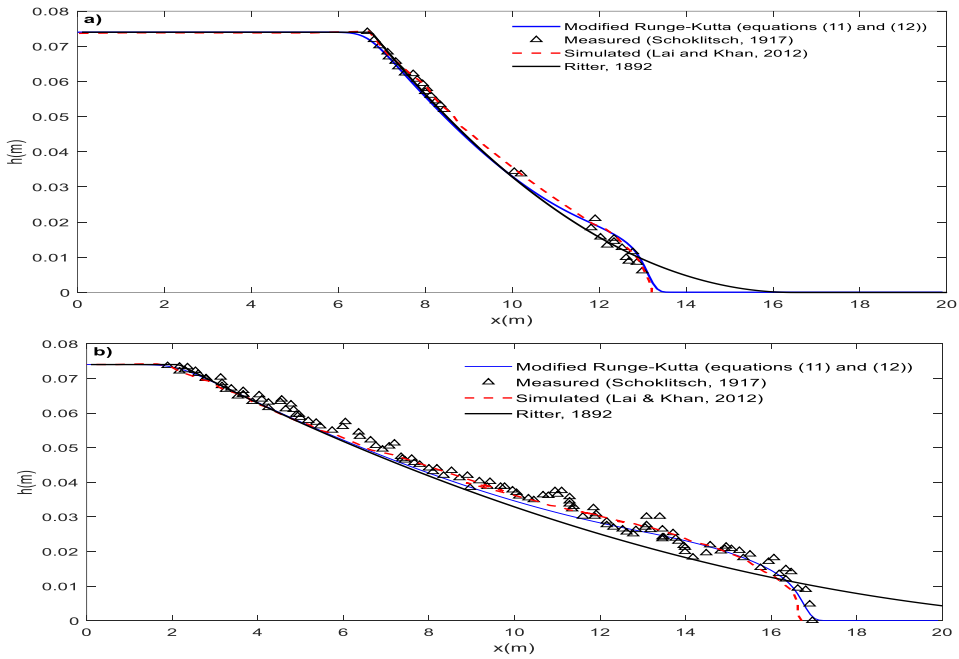

Figure 8: *Water surface profile in the channel after the dam-break phenomenon:* ***a)*** *t=3.75s and* ***b)*** *t=9.40s.*

Slika 8: *Potek gladine vode v kanalu po porušitvi pregrade:* ***a)*** *t=3,75 s in* ***b)*** *t=9,40 s.*

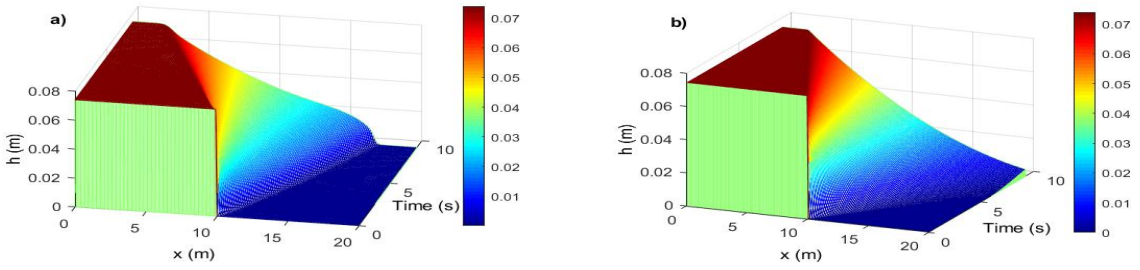

Figure 9*: Simulated and analytical results at t=9.4s: a) three-dimensional variation view in simulated depth h (m) for a real fluid and b) three-dimensional variation view in analytical depth h (m) for an ideal fluid.*

Slika 9*: Simulirani in analitični rezultati pri t=9,4s: a) tridimenzionalni prikaz sprememb v simulirani globini h (m) za realno tekočino in b) tridimenzionalni prikaz sprememb v analitični globini h (m) za idealno tekočino.*

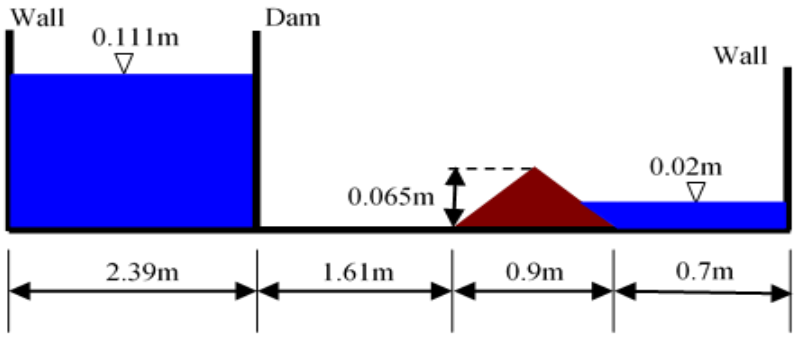

Figure 10: *Dam-break phenomenon with a triangular obstacle.*

Slika 10: *Pojav porušitve pregrade s trikotno oviro.*

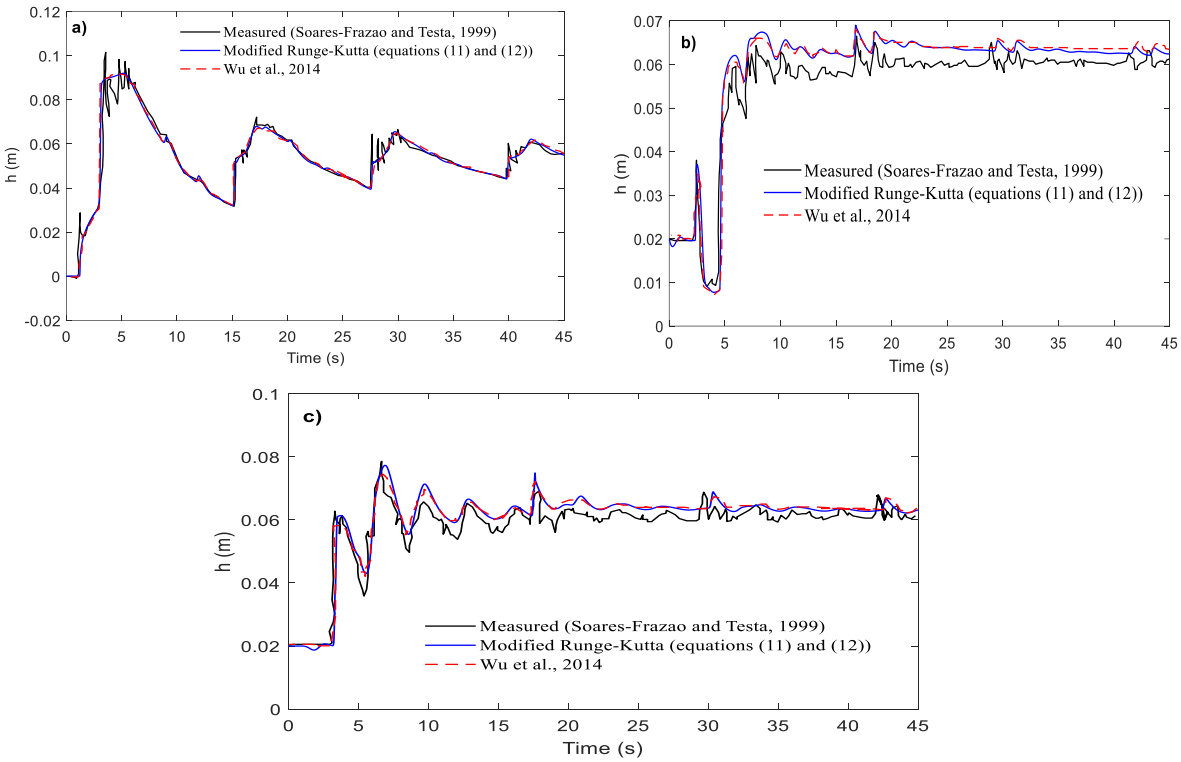

Figure 11: *Variation in water depth at stations according to time:* ***a)*** *G1,* ***b)*** *G2, and* ***c)*** *G3.*

Slika 11: *Spreminjanje globine vode na postajah glede na čas:* ***a)*** *G1,* ***b)*** *G2 in* ***c)*** *G3.*

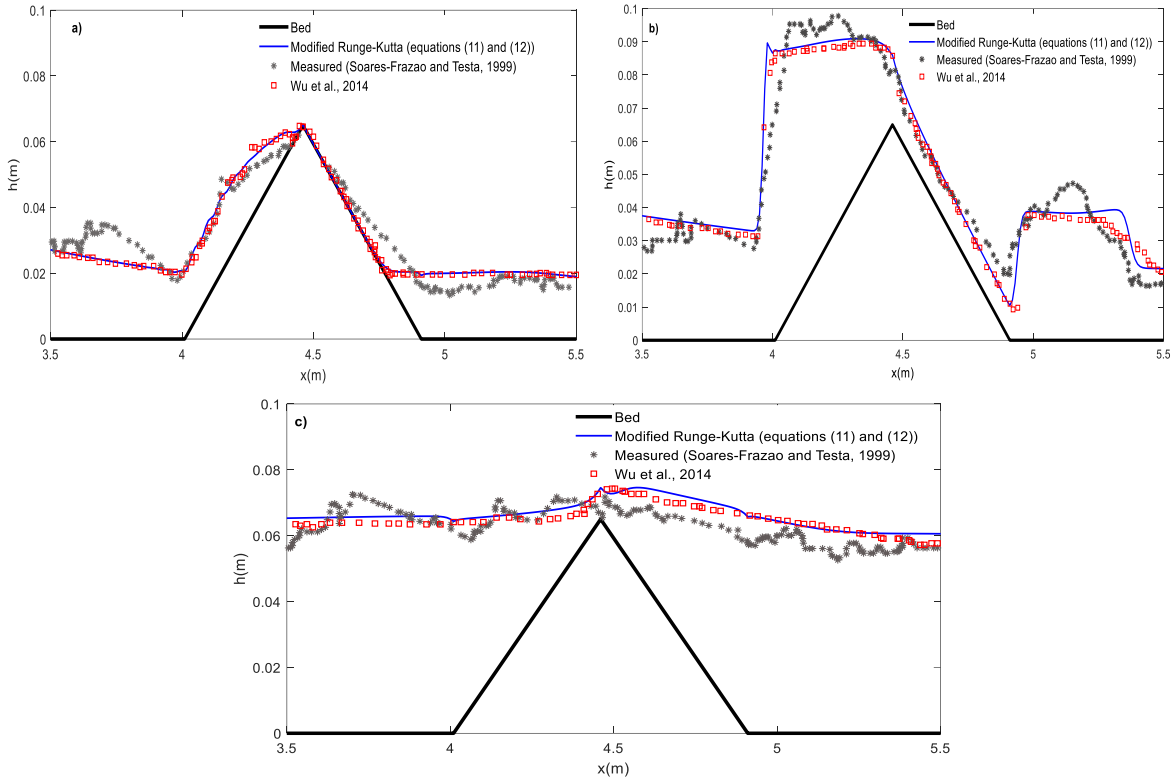

Figure 12: *Water depth variation in the channel in the presence of an obstacle:* ***a)*** *t=2s,* ***b)*** *t=5s, and* ***c)*** *t=8.5s.*

Slika 12: *Spreminjanje globine vode v kanalu ob prisotnosti ovire:* ***a)*** *t=2s;* ***b)*** *t=5s in* ***c)*** *t=8,5s.*

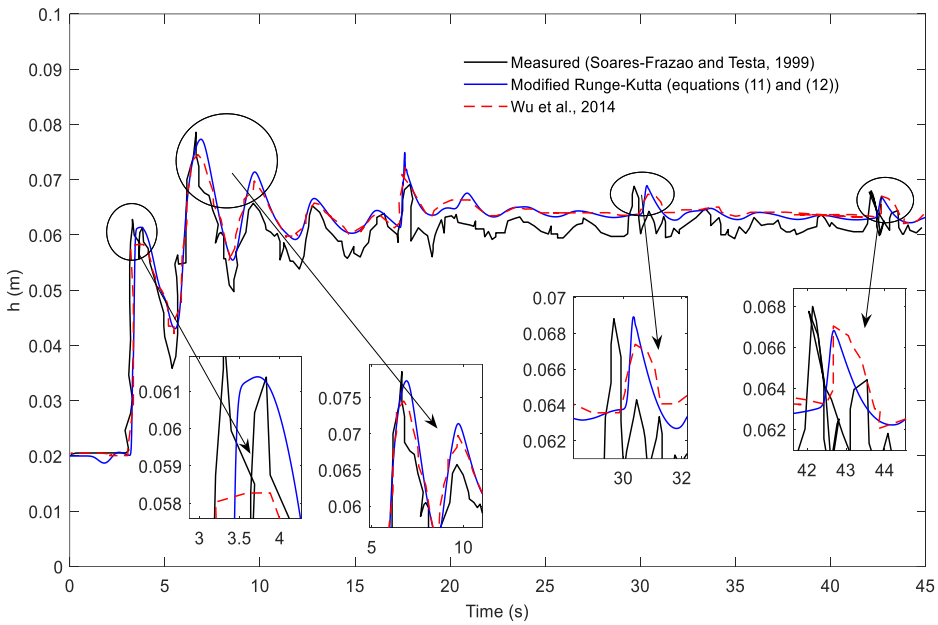

Figure 13: *Comparison between current results and those of Wu et al. (2014).*

Slika 13: *Primerjava med trenutnimi rezultati in rezultati Wu et al. (2014).*

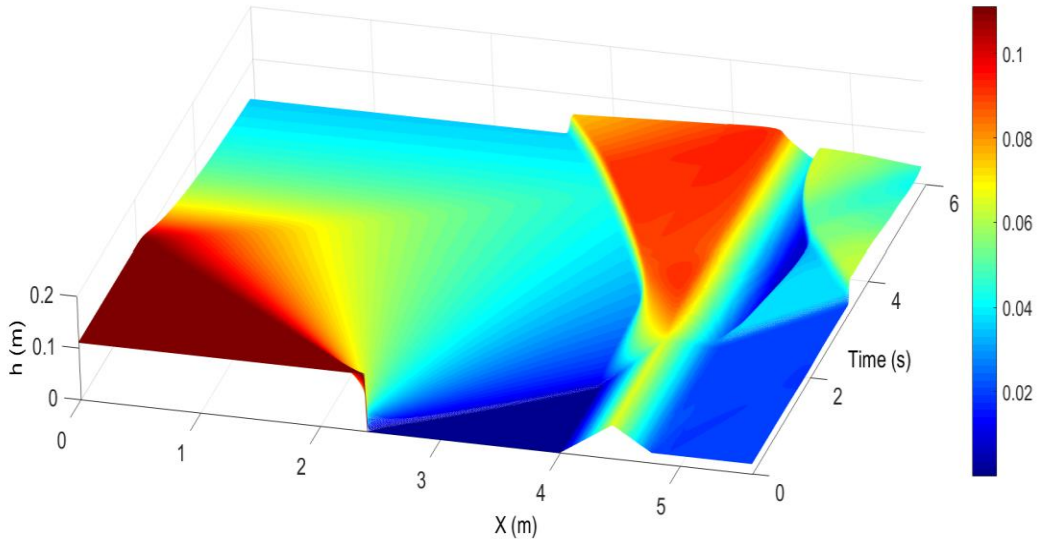

Figure 14: Three-dimensional view of depth variation h(m) at *t*=6 s.

Slika 14: *Tridimenzionalni prikaz spremembe globine h(m) pri t=6 s.*

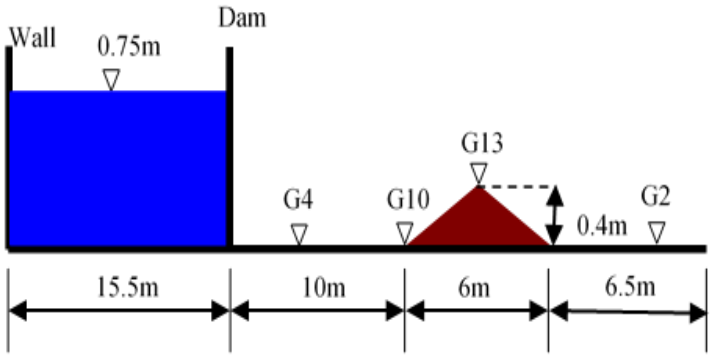

Figure 15: *Dam failure in the case of a triangular obstacle on a dry bottom.*

Slika 15: *Pojav porušitve pregrade v primeru trikotne ovire na suhem dnu.*

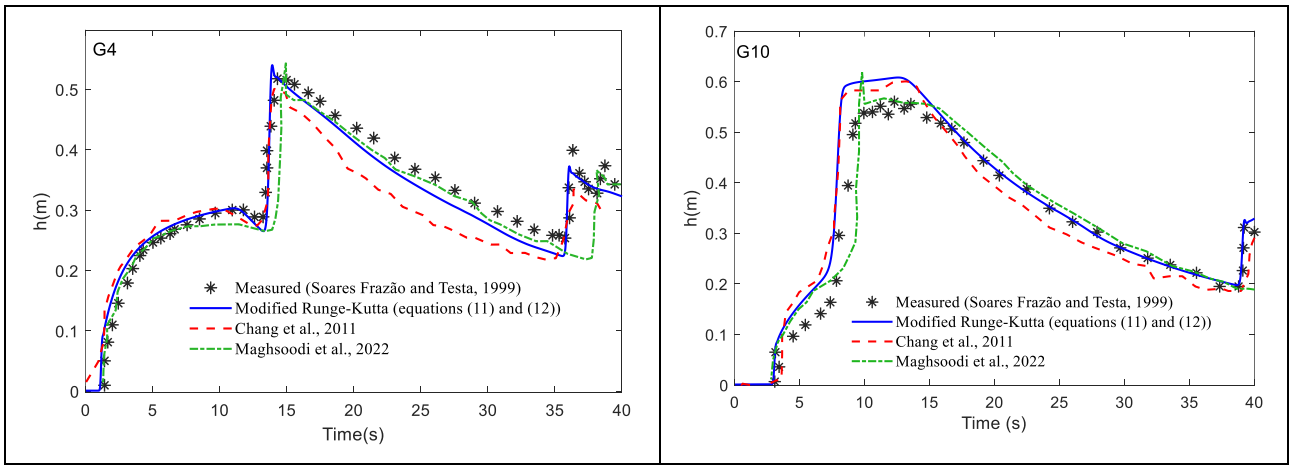

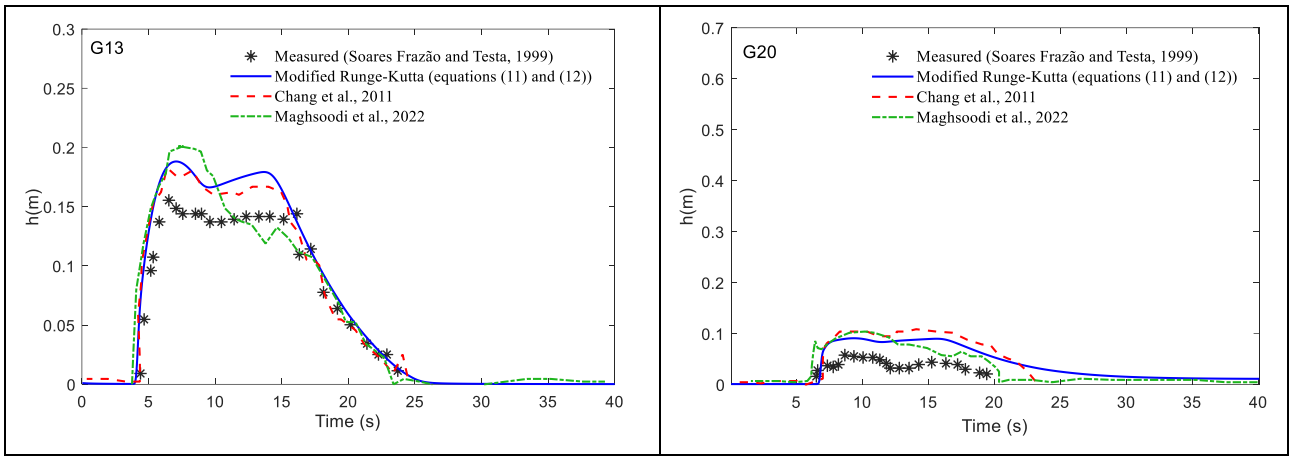

Figure 16: *Water level at station:* ***a)*** *G4 (4m downstream of dam),* ***b)*** *G10 (10m downstream of dam),* ***c)*** *G13 (13m downstream of dam) and* ***d)*** *G20 (20m downstream of dam).*

Slika 16: *Vodostaj na postajah:* ***a)*** *G4 (4 m dolvodno od pregrade),* ***b)*** *G10 (10 m dolvodno od pregrade),* ***c)*** *G13 (13 m dolvodno od pregrade) in* ***d)*** *G20 (20 m dolvodno od pregrade).*

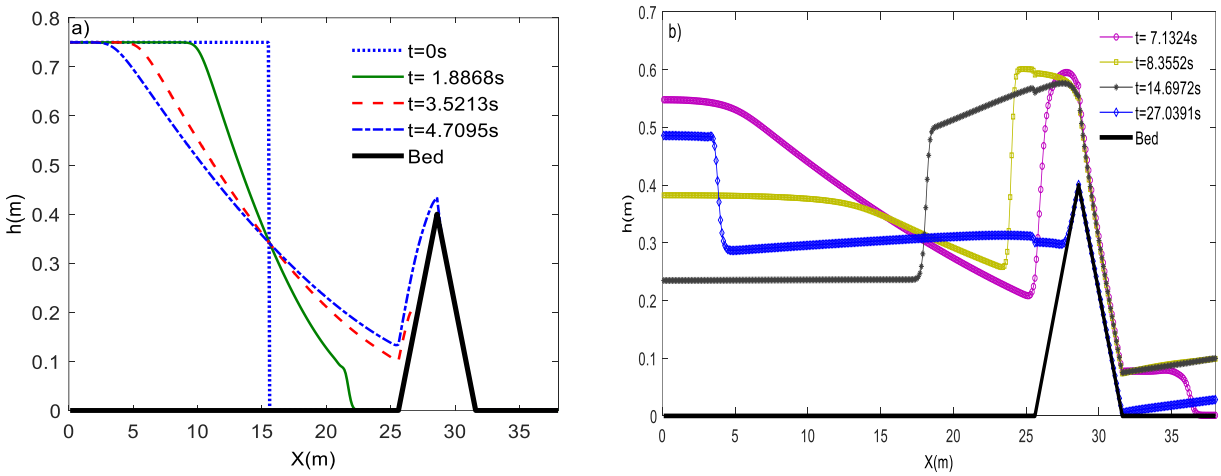

Figure 17: *Water depth variation along the channel at different times.*

Slika 17: *Spreminjanje globine vode vzdolž kanala v različnih časih.*

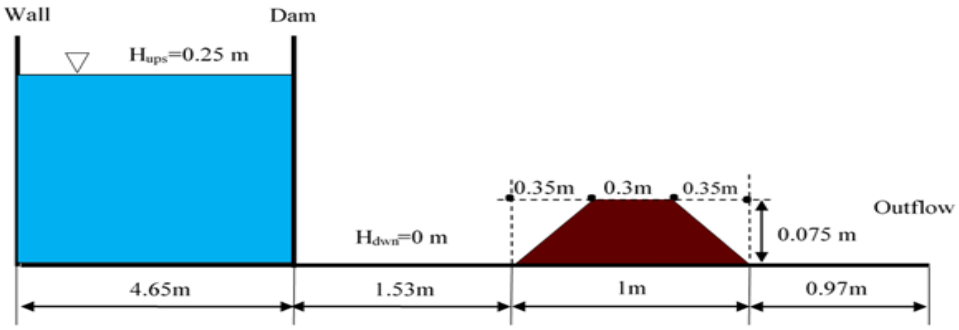

Figure 18: *Dam failure in the case of a trapezoidal obstacle on a dry bottom.*

Slika 18: *Pojav porušitve pregrade v primeru trapezne ovire na suhem dnu.*

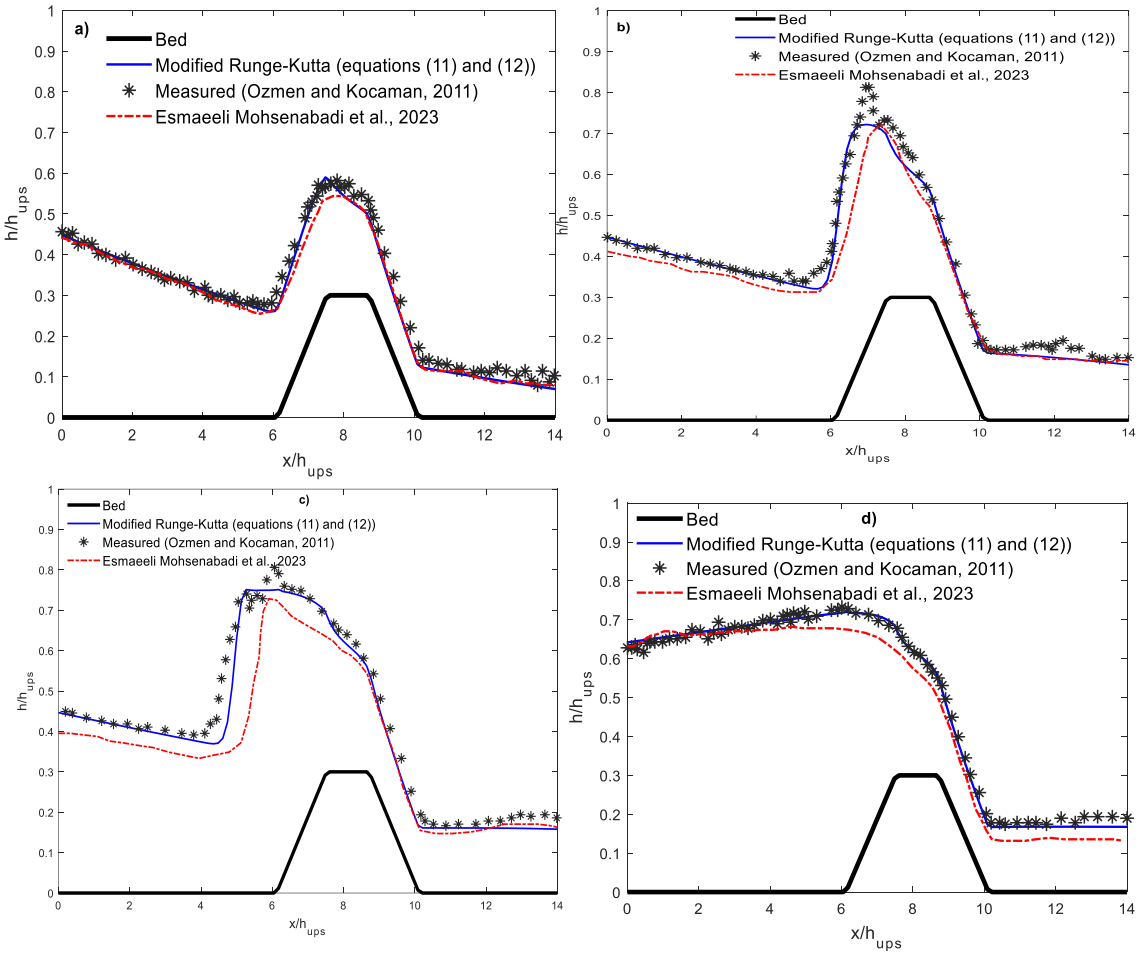

Figure 19*: Dam-break wave propagation on a horizontal surface obstructed by a trapezoidal obstacle: comparison of experimental and computed results at a) t=2.8 s; b)* t=*3.3 s; c) t=4.7 s; d) t=6.7 s.*

Slika 19: *Širjenje vala po porušitvi pregrade na vodoravni površini, trapezno oviro: primerjava eksperimentalnih in izračunanih rezultatov pri a) t=2,8 s; b) t=3,3 s; c) t=4,7 s; d) t=6,7 s.*

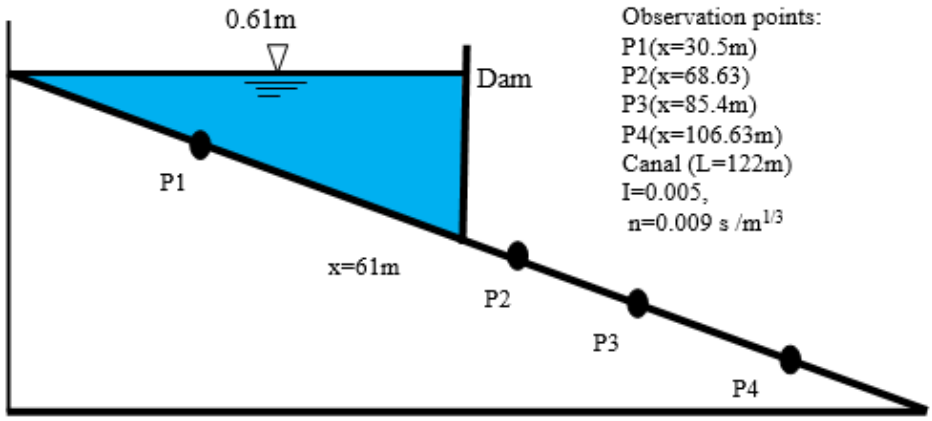

Figure 20: *Initial conditions of the dam failure problem on an inclined channel.*

Slika 20: *Začetni pogoji problema porušitve pregrade va nagnjenem kanalu.*

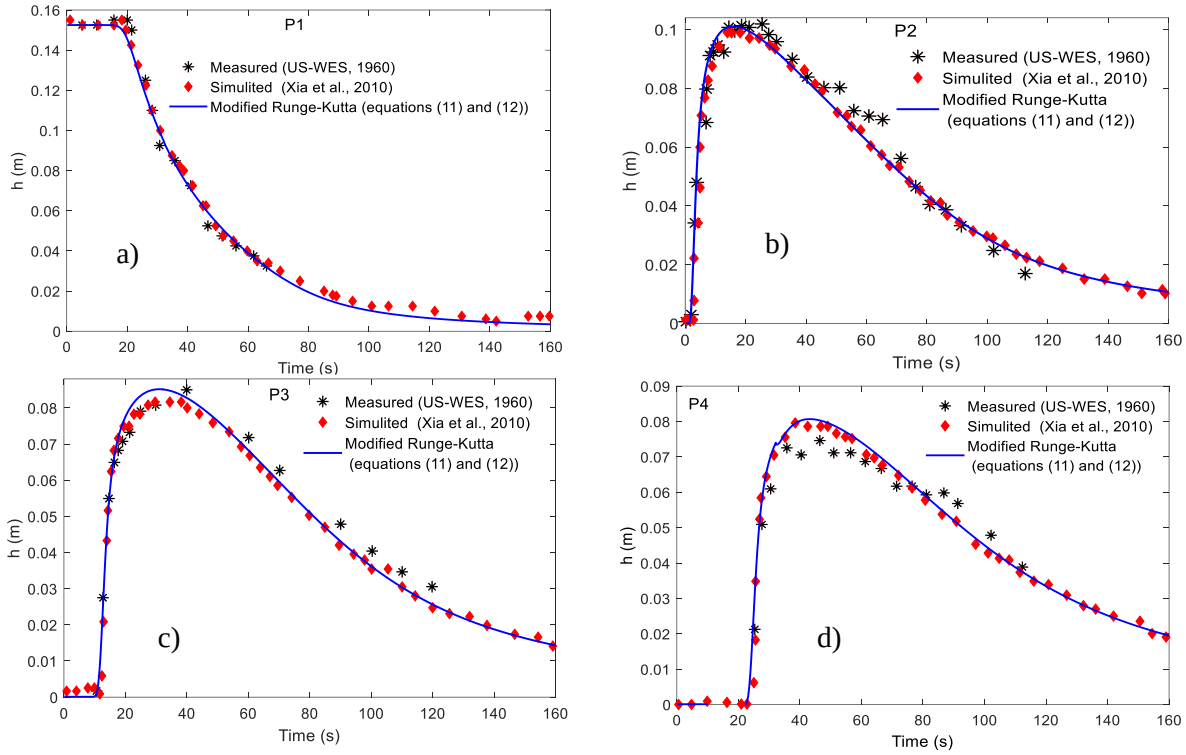

Figure 21: *Comparison of calculated water level with experimental and simulated data (Xia et al., 2010) at the four stations P1, P2, P3, and P4.*

Slika 21: *Primerjava izračunanega nivoja vode z eksperimentalnimi in simuliranimi podatki (Xia et al., 2010) na štirih postajah P1, P2, P3 in P4.*

3.4 Dam-break on a bed in the presence of an obstacle without reflection

Fig. 15 presents an illustration of the dam-break experiment if there is an obstruction. The dam is positioned 15.5 m from the upstream entry to the 38m-long channel. At a location downstream of the dam, a triangle-shaped obstruction measuring 0.4 m high and 6 m wide is placed. Upstream of the dam, the initial water depth is 0.75 m, and the rest of the channel is dry. The experimental points for measuring water height are situated in locations G4 at 4m, G10 at 10m, G13 at 13 m, and G20 at 20 m downstream of the dam. The wide channel is 1.75 m, while the rugosity coefficient utilized is n=0.0125 s.m-$^{1/3}$ (Soares Frazao and Testa, 1999; Maghsoodi et al., 2022).

Fig. 16a shows the water level variation according to time at station G4. This figure clearly shows that the calibration of experimental results with simulated results from the proposed model (equations (11) and (12)) is highly satisfactory. The obtained results using the present model and by Maghsoodi et al. (2022) treated the dam-break wave with ANSYS Fluent 6.3.26 using 3D Reynolds equations. Chang et al. (2011), applied the SPH method to study this fairly dangerous hydraulic phenomenon. The grid is composed of 380 points. The boundaries are solid walls except for the free outlet at the downstream end of the channel. Figure 14 shows the experimental water depth evolution obtained by Soares Frazao and Testa (1999), calculated by Chang et al. (2011) and Maghsoodi et al. (2022), and simulated with the proposed model (equations (11) and (12)). The CFL adopted in the dam-break simulations is 0.95. The number of grid points remains constant (N=380 points).

Maghsoodi et al. (2022) are close and follow the experimental measurements satisfactorily. This curve clearly shows that the obtained results by the numerical model proposed and by Maghsoodi et al.

(2022) are far better than those of Chang et al. (2011).

Fig. 16a shows the water level variation according to time at station G4. This figure clearly shows that the calibration of experimental results with simulated results from the proposed model (equations (11) and (12)) is highly satisfactory. The results obtained using the present model and by Maghsoodi et al. (2022) are close and follow the experimental measurements satisfactorily. This curve clearly shows that the results obtained by the numerical model proposed and by Maghsoodi et al. (2022) are far better than those of Chang et al. (2011).

The variation in height according to time at station G10 is shown in Fig. 16b. In this application, the proposed model (eqs.11 and 12) gives the best fit with the experimental measurements, no matter the simulation time. At the two stations G13 and G20, Figs. 16c and 16d show that the obtained calibration is significantly better than those performed by Chang et al. (2011) and Maghsoodi et al. (2022). The comparison between simulated and experimental measurements clearly shows that the elaborated numerical model is capable of representing unsteady flow behavior fairly well.

Figure 17 shows the variation in water level along the canal at different times. After the dam breaks, the water flows up to the obstacle. Once it reaches the obstacle, part of the wave is reflected upstream, while the other part flows up the obstacle.

3.5 Dam-break in a rectangular channel with a trapezoidal obstacle without reflection

Figure 18 illustrates a dam-break experiment conducted in a horizontal rectangular channel measuring 8.15 m in length, 0.3 m in width, and 0.3 m in height, as reported by Özmen-Cağatay and Kocaman (2011). The dam is located 4.65 m from the upstream end of the channel and retains an initial water depth of 0.25 m, while the downstream section is initially dry. A rigid trapezoidal obstacle is placed 1.53 m downstream of the dam, centered on the channel bed.

The downstream end of the channel is open, allowing the wave to propagate freely without reflection. This setup enables analysis of the interaction between the dam-break wave and a non-submersible obstacle under dry-bed and well-controlled geometric conditions.

Figure 19 shows three sets of results in perspective: the experimental data from the work of Özmen-Cağatay and Kocaman (2011), the numerical simulations carried out by Esmaeeli Mohsenbadi et al. (2023) using OpenFOAM based on the Volume of Fluid method employing the Finite Volume Method, and the numerical results obtained by the numerical model developed in the present study (equations (9) and (10)). The obtained results over the different time periods illustrated in the sub-figures (19.a, 19.b, 19.c and 19.d) show a remarkable agreement between the results of the physical experiment and those produced by the proposed scheme, which attests to its ability to accurately capture the characteristics of the transient flow induced by dam failure, and that the model that we have proposed presents much better results than those produced by Esmaeeli Mohsenbadi et al, (2023) over the different time periods, confirming the improvement.

3.6 Dam failure on an inclined plane

Xia et al (2010) used the dam failure on an inclined plane experiment carried out by US-WES (1960), to validate their numerical model, which is based on solving the 2D Saint-Venant equations using a finite volume method.

The channel used by US-WES is 122 m long and 1.22 m wide. The bottom slope I is 0.005 with a Manning's friction coefficient n=0.0085 s /m1/3. A dam of infinitesimally small thickness, 0.305 m high, is placed midway along the channel. Figure 20 shows the initial conditions.

Boundary conditions: at the upstream end (x=0m), the level of the free surface $h=10^{-6}$ m is imposed and remains unchanged during the calculations. As the flow is supercritical throughout the downstream part of the dam, at the downstream end (x=122 m), the free surface level and velocity are determined by a linear extrapolation method

(Ikni et al., 2024). The number of nodes used is 122 and the CFL used is 0.9. Figure 21 shows the comparison of the water height h(m) obtained by the present model with the experimental and numerical measurements (Xia et al., 2010) at the four stations located upstream and downstream of the dam. Figure 21 also shows a good fit between the experimental results and the simulation results obtained. Figures 21b, 21c, and 21d illustrate that the peaks at the three stations measuring water level versus time (x=68.63m, x=85.4m, and x=106.63m) are well estimated with the current model. At the first station (x=30.5m), the two simulation results are identical

4. Conclusion

The free-surface flow due to the dam-break phenomenon was modelled numerically the present study. The common point in the problems examined is the use of the 1D Barré de Saint-Venant free-surface flow mathematical model. Six scenarios are analyzed in this research paper. In the first scenario, the flow of the dam-break wave in a wet horizontal channel without taking friction into account is studied. On the other hand, the second scenario concerns the case of a horizontal plane channel but with friction. The passage of a flow due to the dam-break problem through a triangular obstacle with reflection is carried out in the third scenario. The fourth scenario considers the same configuration with a triangular obstacle, but without reflection. The fifth case examines the flow generated by the rupture through a trapezoidal obstacle, also without reflection. Finally, the sixth scenario looks at wave propagation in an inclined channel. A comparative study between the classical second-order Runge–Kutta scheme and the new form of the Runge–Kutta scheme after decomposing the flux term was carried out to compute the dam-break. The numerical precision is perfectly proved by applying the new expression of the Runge–Kutta method to simulate this phenomenon. The numerical simulations discussed above and the calculated relative error allow us to conclude that the proposed new formulation of the Runge–Kutta scheme is efficient for the simulating the 1D dam-break problem regardless of the flow regime, including the presence of obstacles.

CRediT authorship contribution statement

- [TOUAZI Lamia 1]: PhD Student, this work falls under my thesis topic. I designed, developed, modelled, and conducted the study, and I further wrote and revised the article.

- [IKNI Tahar 2]: Thesis co-director, whose contribution is significant in the results and discussion section, and he made critical revisions to the manuscript.

- [BERREKSI Ali 3]: Thesis director, his contribution is in the modeling and equating part, and provided essential advice that optimized the writing and formatting of the article.

All authors have read and approved the final version of the manuscript and there are no conflicts of interest.

Data availability

The data used and analyzed in this study originate from our own programming and were compared with previous works from the specialized literature. These data are available and can be provided by the corresponding author upon reasonable request.

Declaration of interest

The authors confirm that there are no known financial or personal conflicts of interest that could have affected the objectivity or integrity of the work presented in this article. Additionally, no generative artificial intelligence tools were used in the drafting or preparation of the manuscript.

Funding

This research received no funding from public, commercial, or non-profit organizations.

References

Al-Ansari, N.; Adamo, N.; Issa, I. E.; Sissakian, V. K.; Knutsson, S. (2015). Mystery of Mosul Dam the Most Dangerous Dam in the World: Dam Failure and its Consequences, *Journal of Earth Sciences and Geotechnical Engineering*, 5(3), 95-111.

Azeez, O.; Elfeki, A.; Kamis, A. S.; Chaabani, A. (2020). Dam-break analysis and flood disaster simulation in arid urban environment: the Um Al-Khair dam case study, Jeddah, Saudi Arabia. Natural Hazards, 100(3), 995-1011. https://doi.org/10.1007/s11069-019-03836-5.

Bellos, V.; Hrissanthou, V. (2011). Numerical simulation of a dam-break flood wave, *European Water*, 33, 45-53.

Berreksi, A.; Ikni, T.; Benmamar, S.; Amara, L.; Hamchaoui, S.; Benzerra, A.; Remini, B. (2022). Numerical study using an implicit finite difference scheme of a high velocity flow crossing a non-prismatic hydraulic structure – case of symmetrical gradual expansion, International *Journal of Hydrology Science and Technology*, 14(2), 109–123. doi: 10.1504/IJHST.2022.124544.

Cannata, M.; Marzocchi, R. (2012). Two-dimensional dam break flooding simulation: a GIS-embedded approach, *Natural Hazards*, 61, 1143-1159. https://doi.org/10.1007/s11069-011-9974-6

Castro-Orgaz, O.; Chanson, H. (2017). Ritter's dry-bed dam-break flows: positive and negative wave dynamics, *Environmental Fluid Mechanics*, 17, 665-694, https://doi.org/10.1007/s10652-017-9512-5

Chang, T. J.; Kao, H. M.; Chang, K. H.; Hsu, M. H. (2011). Numerical simulation of shallow-water dam break flows in open channels using smoothed particle hydrodynamics, *Journal of Hydrology*, 408(1-2), 78-90.

Chanson, H. (2004). The Hydraulics of Open Channel Flows: An Introduction. Butterworth-Heinemann, Oxford, UK, 2nd edition, 630 p.

Chanson, H. (2005). Applications of the Saint-Venant equations and method of characteristics to the dam break wave problem, Report No. CH55/05, Department of Civil Engineering, The University of Queensland, Brisbane, Australia, May, 135 p. https://doi.org/10.14264/9438

Chen, A. S.; Hsu, M. H.; Chen, T. S.; Chang, T. J. (2005). An integrated inundation model for highly developed urban areas, *Water Science and Technology*, 51, 221-229.

Das, S. K.; Bagheri, J. (2015). Modelling of shallow-water equations by using compact MacCormack-type schemes with application to dam-break problem, International *Journal of Advances in Applied Mathematics and Mechanics*, 2(3), 60-71.

García-Martínez, R.; González-Ramírez, H.; O'Brien, J. S. (2009). Dam-break flood routing. WIT Transactions on State of the Art in Science and Engineering, Vol. 36. WIT Press, Southampton, UK. ISSN 1755-8336 (online). https://doi.org/10.2495/978-1-84564-142-9/04.

García-Navarro, P.; Brufau, P.; Burguete, J.; Murillo, J. (2008). The shallow water equations: An example of hyperbolic system. Monografias de la Real Academia de Ciencias de Zaragoza, Fluid Mechanics, CPS. University of Zaragoza. 50018 Zaragoza, Spain, 31, 89-119.

Gu, S.; Zheng, X.; Ren, L.; Xie, H.; Huang, Y.; Wei, J.; Shao, S. (2017). SWESPHysics simulation of dam break flows at South-Gate Gorges Reservoir, *Water*, 9(6), 387-407. https://doi.org/10.3390/w9060387

Hsu, C.-T.; Yeh, K.-C. (2002). Iterative explicit simulation of 1D surges and dam-break flows, International *Journal of Numerical Methods in Fluids*, 38, 647-675, https://doi.org/10.1002/fld.236.

Ikni, T.; Berreksi, A.; Hamidou, M.; Belhocine, M.; Nebbar, M. L.; Benkadja, R. (2018). Contribution to the study of the dam break wave propagation via finite differences formulations, *Larhyss Journal*, 33, 169-188.

Ikni, T.; Berreksi, A.; Touazi, L.; Belhocine, M. (2024a). Lax-Friedrichs numerical scheme for simulating the failure wave of a dam in the presence of obstacles, *Larhyss Journal*, 57, 175-185.

Ikni, T.; Berreksi, A.; Bennacer, L. (2024b). One-dimensional numerical simulation of dam failure, Studies in Engineering and Exact Sciences, 5(2), 1-22.

IMPACT, EC Contract EVG1-CT-2001-00037. Investigation of Extreme Flood Processes and Uncertainties, 2004, http://www.impact-project.net/.

Kirstetter, G.; Delestre, O.; Lagree, P.-Y.; Popinet, S.; Josserand, C. (2021). B-flood 1.0: an open-source Saint-Venant model for flash flood simulation using adaptive refinement, *Geosientific Model Development Discussions*, https://doi.org/10.5194/gmd-2021-15

Lai, W.; Khan, A. A. (2012). Discontinuous Galerkin Method for 1D Shallow Water Flows in Natural Rivers, *Engineering Applications of Computational Fluid Mechanics*, 6, 1, 74-86, https://doi.org/10.1080/19942060.2012.11015404

Lim, M.; Ginting, B. M.; Senjaya, T.; Kieswanti, C. (2024). Comparison of 1D, coupled 1D–2D, and 2D shallow water numerical modeling for dam-break flow analysis of Way-Ela dam, Indonesia. *Acta Hydrotechnica*, 27-50. https://doi.org/10.15292/acta.hydro.2024.02

Magdalena, I.; Pebriansyah, M. F. E. (2022). Numerical treatment of finite difference method for solving dam break model on a wet-dry bed with an obstacle. *Results in Engineering*, 14, 100382.

Maghsoodi, R.; Khademalrasoul, A.; Sarkardeh, H. (2022). 3D numerical simulation of dam-break flow over different obstacles in a dry bed, *Water Supply*, 22(4), 4015. https://doi.org/10.2166/ws.2022.031.

Maitsa, T.-R.; Mardika, M.-G.-I.; Adityawan, M.-B.; Harlan, D.; Kusumastuti, D.; Kuntoro, A.-A. (2020). 2D numerical simulation of urban dam break and its effect to building using Lax scheme with numerical *filter*. *E3S Web of Conferences*, 156, 04003. https://doi.org/10.1051/e3sconf/202015604003.

Mohapatra, P.K.; Bhallamudi, S.M. (1996). Computation of a dam-break flood wave in channel transitions, *Advances in Water Resources*, 19(3), 181–187,

Mohsenabadi, S. E.; Nistor, I.; Mohammadian, A.; Kheirkhah Gildeh, H. (2023). CFD modelling of initial stages of dam-break flow, *Canadian Journal of Civil Engineering*, 50(10), 838–852. https://doi.org/10.1139/cjce-2021-0493

Ozmen Cagatay, H.; Kocaman, S. (2011). Dam-Break Flow in the Presence of Obstacle: Experiment and CFD Simulation, *Engineering Applications of Computational Fluid Mechanics*, 5(4), 541–552. https://doi.org/10.1080/19942060.2011.11015393

Pilotti, M.; Maranzoni, A.; Tomirotti, M.; Valerio, G. (2011). 1923 Gleno Dam break: case study and numerical modelling, *Journal Hydraulic Engineering*, 137(4), 480-492. https://doi.org/10.1061/(ASCE)HY.1943-7900.0000327

Rahou, I.; Korichi, K. (2023). Comparative analysis of numerical solutions of 2D unsteady dam break waves using FVM and SPH method. *Journal of Hydrology and Hydromechanics*, 71(3), 305-315. https://doi.org/10.2478/johh-2023-0005

Ritter, A. (1892). Die fortpfazung der wasser-wellen Zeitschrift des Vereins, Deutscher Ingenieure. 36(33), 947-954.

Schoklitsch, A. (1917). Ueber Dammbruchwellen. Sitzungsberichte der Kaiserlichen Akademie Wissenschaften, Viennal, 126, 1489-1514.

Soares Frazao, S.; Testa, G. (1999). The Toce River test case: numerical results analysis. In: Proceedings of the 3rd CADAMWorkshop, Milan, Italy.

Soleymani, S.; Golkar, H.; Yazid, H.; Tavousi, M. (2015). Numerical modeling of dam failure phenomenon using software and finite difference method, *Journal of Materials and Environmental Science*, 6(11), 3143-3158.

Stoker, J. J. (1957). Water Waves. Interscience Publishers Inc., Wiley and Sons, New York, NY, U.S.A.

Torbi, H.; Boushaba, F.; Yachoutti, A.; Salhi, N. (2019). Numerical modeling of dam-break problems 1-D on dry bed, *ICAMOP Journal*, 1(1), 29–32.

Tseng, M.-H., and Chu, C.-R. (2000). "The simulation of dam-break flows by an improved predictor–corrector TVD scheme." Advances in Water Resources, 23(7), 637–643. https://doi.org/10.1016/S0309-1708(99)00051-2

U.S. Waterways Experiment Station (WES), 1960. Investigation of flow caused by sudden release of water in a horizontal rectangular channel. Technical Report No. 2-144, Vicksburg, Mississippi, USA.

Wu, G.; He, Z.; Liu, G. (2014). Development of a Cell-Centered Godunov-Type Finite Volume Model for Shallow Water Flow Based on Unstructured Mesh, Mathematical Problems in Engineering, 2014, 257915, http://dx.doi.org/10.1155/2014/257915.

Xia, J.; Falconer, R. A.; Lin, B.; Tan, G. (2010). Modelling flood routing on initially dry beds with the refined treatment of wetting and drying, *International Journal of River Basin Management*, 8(3–4), 225–243. https://doi.org/10.1080/15715124.2010.502121

You, L.; Li, C.; Min, X.; Xiaolei, T. (2012). Review of Dam-break Research of Earth-rock Dam Combining with Dam Safety Management, Procedia Engineering, 28, 382–388. https://doi.org/10.1016/j.proeng.2012.01.737.

Zendrato, N.-L.-H.; Harlan, D.; Adityawan, M.-B. S.; Natakusumah, D.-K. (2019). *1D numerical modelling of dam break using finite element method*. *MATEC Web of Conferences*, 270, 04022. https://doi.org/10.1051/matecconf/201927004022.

Zokagoa, J.-M.; Soulaïmani, A. (2010). Modeling of wetting–drying transitions in free-surface flows over complex topographies, *Computer Methods in Applied Mechanics and Engineering*, 199, 2281-2304.